Filtered Two-Fluid Models of Fluidized Gas-Particle Flows: New Constitutive Relations

Christian C. Milioli, Fernando E. Milioli, William Holloway, Kapil Agrawal, and Sankaran Sundaresan
Dept. of Chemical and Biological Engineering, Princeton University, Princeton, NJ 08544

DOI 10.1002/aic.14130
Published online May 22, 2013 in Wiley Online Library (wileyonlinelibrary.com)

New constitutive relations for filtered two-fluid models (TFM) of gas-particle flows are obtained by systematically filtering results generated through highly resolved simulations of a kinetic theory-based TFM. It was found in our earlier studies that the residual correlations appearing in the filtered TFM equations depended principally on the filter size and filtered particle volume fraction. Closer inspection of a large amount of computational data gathered in this study reveals an additional, systematic dependence of the correction to the drag coefficient on the filtered slip velocity, which serves as a marker for the extent of subfilter-scale inhomogeneity. Furthermore, the residual correlations for the momentum fluxes in the gas and particle phases arising from the subfilter-scale fluctuations are found to be modeled nicely using constitutive relations of the form used in large-eddy simulations of single-phase turbulent flows. © 2013 American Institute of Chemical Engineers *AIChE J*, 59: 3265-3275, 2013

Keywords: multiphase flows, gas-particle flow, two-fluid model, coarse grid simulation, constitutive relations, filtered model, kinetic theory of granular flows

Introduction

Persistent fluctuations in particle volume fraction and the local-average velocities of the gas and particle phases occur in turbulent and circulating fluidized beds. These fluctuations span a wide range of length and time scales, and so are both difficult and expensive to resolve in simulations.[1] Filtered two-fluid model (TFM) approaches aim to resolve only the coarse, macroscale flow structures which are usually of most interest in practical applications. The effects of unresolved subfilter-scale structures appear in the filtered models through residual correlations, which must be constituted in terms of the filtered variables.

In our earlier studies,[1–6] we performed highly resolved simulations of a kinetic theory-based TFM with Wen and Yu drag law[7] for uniformly sized particles in large periodic domains and in channels bounded by vertical walls, and filtered the results (using various filter lengths) to obtain computational data on the residual correlations appearing in the filtered TFM. These data were then used to construct closure relationships for the filtered drag coefficient and the filtered stresses in the particle phase. Igci et al.[3] found that the dimensionless filtered fluid-particle drag coefficient, particle-phase pressure, and particle-phase viscosity depended principally on the dimensionless filter size and the filtered volume fraction. With this in mind, they determined the ensemble-average values of these filtered quantities as functions of filtered particle volume fraction, for each (dimensionless) filter size. Thus, the ensemble-average value of, say, the filtered fluid-particle drag coefficient for a specified filter size and in a specific window of filtered particle volume fraction was obtained by sampling a very large number of inhomogeneous subfilter-scale flow structures. Corrections to the drag coefficient proposed by Parmentier et al.[8] are also in terms of the filter size and the particle volume fraction, although the scaling used by them to make the filter size dimensionless differed from that of Igci et al.[3] The shape of the correction function applicable to large filter sizes is very similar in both of these studies. In both of these studies, it was assumed that the inhomogeneous states within this sample could not be subdivided further into different categories based on additional markers such as filtered fluid-particle slip velocity, the filtered scalar shear of the fluid or the particle phase, and so forth. The same assumption applies for the filtered particle-phase pressure and viscosity models proposed by Igci et al.[3] Igci and Sundaresan[4] found that all the closure expressions should be corrected in the vicinity of bounding walls and, therefore, introduced the dimensionless distance from the wall as an additional parameter. It should be noted that the need to correct the drag coefficient has been recognized by Li and coworkers much earlier (e.g., see Ref. 9–11); their studies led to the development of energy minimization multiscale model, in which the filter size does not appear as a parameter. Their model may be viewed as being analogous to the models of Igci et al.[3] and Parmentier et al.[8] in the limit of large filter size.

In this study, we focus on regions away from solid boundaries and investigate additional markers that may be important in further classifying the subfilter-scale structures. To address this, we have performed a large number of simulations of gas-particle flows in periodic domains and classified

Correspondence concerning this article should be addressed to S. Sundaresan at sundar@princeton.edu.
Current address of Fernando E. Milioli: Department of Mechanical Engineering, School of Engineering of São Carlos, University of São Paulo, Brazil.

the filtered results using a variety of markers (in addition to the filter size and the filtered particle volume fraction aforementioned). The additional marker serves to classify the inhomogeneous subfilter-scale flow structures into different groups. Several different choices for this additional marker were examined by classifying the subgrid-scale structures obtained for a given filter size in terms of the filtered particle volume fraction and the chosen second marker. The average values of the filtered quantities in each of such two-dimensional (2-D) bins were then determined and analyzed to see if the filtered quantity manifested any systematic dependence on the chosen second marker. This analysis revealed a surprising result that the filtered drag coefficient (at a given filter size and filtered particle volume fraction) decreased with increasing filtered slip velocity, which at first is counterintuitive, but can be rationalized (discussed below). These findings suggest a more refined model for filtered drag coefficient, the details of which are discussed in this article.

Igci et al.[3] modeled the (dimensionless) filtered particle-phase pressure and viscosity as functions of filtered particle volume fraction and dimensionless filter size. It is shown in this study that the residual correlations for the gas and particle-phases momentum fluxes arising through the subfilter-scale fluctuations can be modeled using constitutive relations of the form used in large-eddy simulations of single-phase turbulent flows;[12] these models involve the scalar shear rates associated with the filtered-phase velocities.

Simulation and Filtering Procedure

As in the earlier studies by Igci et al.,[3] fluidization of particles by a gas in 2-D periodic domains was simulated using a kinetic theory-based TFM. We present below only the continuity and momentum balance equations

$$\frac{\partial}{\partial \mathrm{t}}(\rho_\mathrm{s}\phi_s)+\nabla\cdot(\rho_\mathrm{s}\phi_s\mathbf{v}_s)=0 \tag{1}$$

$$\frac{\partial}{\partial \mathrm{t}}\left(\rho_\mathrm{g}\phi_g\right)+\nabla\cdot\left[\rho_\mathrm{g}\phi_g\mathbf{v}_g\right]=0 \tag{2}$$

$$\left[\frac{\partial}{\partial \mathrm{t}}(\rho_\mathrm{s}\phi_s\mathbf{v}_s)+\nabla\cdot(\rho_\mathrm{s}\phi_s\mathbf{v}_s\mathbf{v}_s)\right]=-\nabla\cdot\sigma_s-\phi_s\nabla\cdot\sigma_g +\beta_\mathrm{micro}\left(\mathbf{v}_g-\mathbf{v}_s\right)+\rho_\mathrm{s}\phi_s\mathbf{g} \tag{3}$$

$$\left[\frac{\partial}{\partial \mathrm{t}}\left(\rho_g\phi_g\mathbf{v}_g\right)+\nabla\cdot\left(\rho_g\phi_g\mathbf{v}_g\mathbf{v}_g\right)\right]=-\phi_g\nabla\cdot\sigma_g -\beta_\mathrm{micro}\left(\mathbf{v}_g-\mathbf{v}_s\right)+\rho_g\phi_g\mathbf{g} \tag{4}$$

Here, ρ_s and ρ_g denote the densities; ϕ_s and ϕ_g denote the phase volume fractions (which add up to unity); $\mathbf{v}_s$ and $\mathbf{v}_g$ are the local-average velocities appearing in the microscopic TFM; σ_s and σ_g are the stress tensors associated with the two phases; $\mathbf{g}$ is the gravitational acceleration; and β_micro is the drag coefficient. The particle-phase stress is closed using the kinetic theory,[13–15] which requires an additional equation for the granular temperature. The granular energy balance equation, the constitutive models employed for the stresses, and the Wen and Yu model for the drag coefficient used in our simulations can be found in Table 1 of Igci et al.[3] and will not be repeated here.

The derivation of the filtered model equations and the residual correlations requiring constitutive models can be found in Igci et al.[3] and we simply summarize the results. An overbar on top of a variable denotes the filtered value,

Table 1. Physical Properties of Gas and Solids

d	Particle diameter	7.5×10^{-5} m
ρ_s	Particle density	1500 kg/m^3
ρ_g	Gas density	1.3 kg/m^3
μ_g	Gas viscosity	1.8×10^{-5} kg/m s
e_p	Coefficient of restitution	0.9
$\mathrm{v_t}$	Terminal settling velocity	0.2184 m/s

and primed quantities indicate difference between the local value of a variable and the corresponding filtered quantity; for example, $\phi'_s=\phi_s-\overline{\phi}_s$. Favre-averaged quantities are denoted with tilde on top: $\tilde{\mathbf{v}}_g=\frac{\overline{\phi_g\mathbf{v}_g}}{\overline{\phi}_g}$; $\tilde{\mathbf{v}}_s=\frac{\overline{\phi_s\mathbf{v}_s}}{\overline{\phi}_s}$. For the velocities, $\mathbf{v}'_i=\mathbf{v}_i-\tilde{\mathbf{v}}_i$; $i=g,s$.

The filtered continuity and momentum balances can be summarized as

$$\frac{\partial}{\partial \mathrm{t}}\left(\rho_\mathrm{s}\overline{\phi_s}\right)+\nabla\cdot\left(\rho_\mathrm{s}\overline{\phi_s}\ \tilde{\mathbf{v}}_s\right)=0 \tag{5}$$

$$\frac{\partial}{\partial \mathrm{t}}\left(\rho_g\overline{\phi_g}\right)+\nabla\cdot\left(\rho_g\overline{\phi_g}\ \tilde{\mathbf{v}}_g\right)=0 \tag{6}$$

$$\frac{\partial}{\partial \mathrm{t}}\left(\rho_s\overline{\phi_s}\tilde{\mathbf{v}}_s\right)+\nabla\cdot\left(\rho_s\overline{\phi_s}\tilde{\mathbf{v}}_s\tilde{\mathbf{v}}_s\right)=-\nabla\cdot\overline{\sigma_s}-\nabla\cdot\overline{\Sigma_{s,\mathrm{fil}}}-\overline{\phi_s}\nabla\cdot\overline{\sigma}_g +\beta_\mathrm{fil}\left(\tilde{\mathbf{v}}_g-\tilde{\mathbf{v}}_s\right)+\rho_\mathrm{s}\overline{\phi_s}\mathbf{g} \tag{7}$$

$$\frac{\partial}{\partial \mathrm{t}}\left(\rho_g\overline{\phi_g}\tilde{\mathbf{v}}_g\right)+\nabla\cdot\left(\rho_g\overline{\phi_g}\tilde{\mathbf{v}}_g\tilde{\mathbf{v}}_g\right)=-\nabla\cdot\overline{\Sigma_{g,\mathrm{fil}}}-\overline{\phi_g}\nabla\cdot\overline{\sigma}_g -\beta_{fil}\left(\tilde{\mathbf{v}}_g-\tilde{\mathbf{v}}_s\right)+\rho_g\overline{\phi_g}\mathbf{g} \tag{8}$$

Here

$$\begin{aligned}&\overline{\Sigma_{i,\mathrm{fil}}}=\rho_i\left(\overline{\phi_i\mathbf{v}_i\mathbf{v}_i}-\overline{\phi_i}\tilde{\mathbf{v}}_i\tilde{\mathbf{v}}_i\right)=p_{i,\mathrm{fil}}\ I-\boldsymbol{\tau}_{i,\mathrm{fil}}\\ &p_{i,\mathrm{fil}}=\frac{1}{3}tr\left(\overline{\Sigma_{i,\mathrm{fil}}}\right),\quad \tau_{i,\mathrm{fil}}=-\overline{\Sigma_{i,\mathrm{fil}}}+\frac{1}{3}tr\left(\overline{\Sigma_{i,\mathrm{fil}}}\right)I\\ &|\tau_{i,\mathrm{fil}}|=\sqrt{\frac{1}{2}\left(\boldsymbol{\tau}_{i,\mathrm{fil}}:\boldsymbol{\tau}_{i,\mathrm{fil}}\right)},\quad \mu_{i,\mathrm{fil}}=\frac{|\boldsymbol{\tau}_{i,\mathrm{fil}}|}{\overline{s_i}},\quad i=s,g\end{aligned} \tag{9}$$

The above model does not consider filtered bulk viscosities. Filtered scalar shear rate of the particle and gas phases are defined as follows

$$\overline{s}_i=\sqrt{2\overline{s}_i:\overline{s}_i},\quad \overline{s}_i=\frac{1}{2}\left(\nabla\tilde{\mathbf{v}}_i+\nabla\tilde{\mathbf{v}}_i^T\right)-\frac{1}{3}(\nabla\cdot\tilde{\mathbf{v}})I,\quad i=s,g \tag{10}$$

The filtered drag coefficient is defined according to

$$\beta_\mathrm{fil}\left(\tilde{\mathbf{v}}_g-\tilde{\mathbf{v}}_s\right)=\overline{\beta_\mathrm{micro}\left(\phi_s,|\mathbf{v}_g-\mathbf{v}_s|\right)\left(\mathbf{v}_g-\mathbf{v}_s\right)}-\overline{\phi'_s\nabla\cdot\sigma'_g} \tag{11}$$

As discussed in Igci et al.,[3] $\overline{\sigma_s}$ contributes very little to the right hand side of Eq. 7 and can be neglected for filters that are two or more orders of magnitude larger than the particle diameter (except near packed-bed conditions). Furthermore, $\nabla\cdot\overline{\sigma}_g$ may be approximated as $\nabla\overline{p}_g$. Thus, the quantities that must be constituted are β_fil, $p_{i,\mathrm{fil}}$ and $\mu_{i,\mathrm{fil}}$, $i=s,g$.

All the simulations were performed using the open-domain, Multiphase Flow with Interphase eXchanges (MFIX)[16] platform developed at the National Energy Technology Laboratory. MFIX is used widely for gas-particle flow simulations and has been verified extensively.[16] We have used it for all of our earlier studies as well. Details of the theory and numerical procedure used in MFIX can be found in the Ref. 16. Second-order accurate superbee discretization for

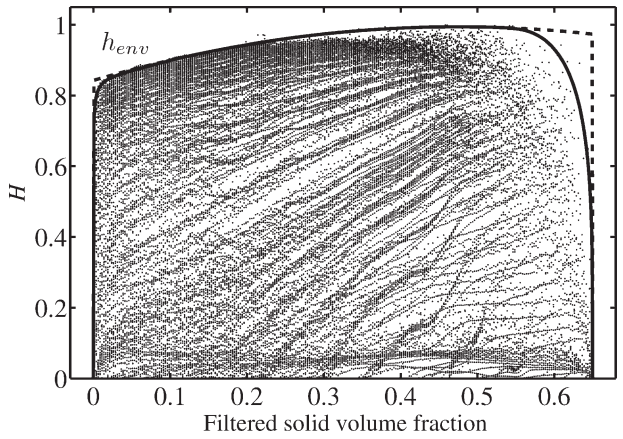

Figure 1. Scatter plot of the correction to the drag coefficient (*H*).

The solid line stands for an approximate envelop of all data $h_{\mathrm{env},1}(\overline{\phi}_s)$. The broken line stands for a simpler envelop, $h_{\mathrm{env},2}(\overline{\phi}_s)$. The simulations were carried out for domain-average solid volume fractions of 0.05, 0.10, 0.15, 0.25, 0.30, 0.35, 0.40, 0.45, 0.50, and 0.55. The dimensionless size of the domain = 131.58 × 131.58. The grid resolution in all the simulations was 0.257 (i.e., 512 × 512 grids). Each point corresponds to a different $\overline{\phi}_s$, $\tilde{\mathrm{V}}_{\mathrm{slip}}$ and Δ_f.

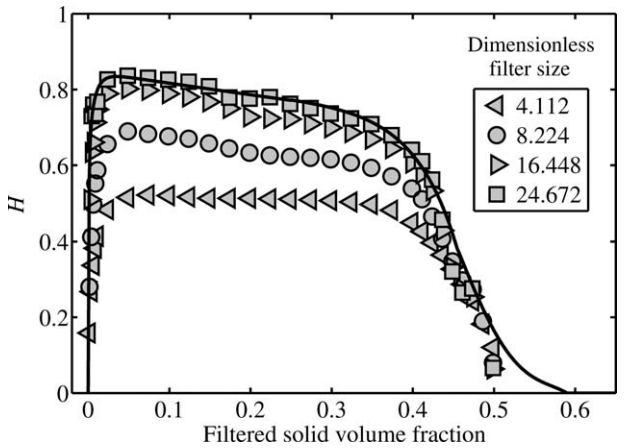

Figure 2. Correction to the drag coefficient, $\langle H\rangle_{\mathrm{inf}}(\overline{\phi}_s)$, obtained by averaging over the filtered slip velocity for different filter sizes.

The solid line is the correction recommended by Igci and Sundaresan[5] for very large filter sizes. The simulation conditions are as in Figure 1.

spatial derivatives and implicit Euler method for time stepping were applied; these are standard options available in MFIX. Simulations were performed in 2-D periodic domains; periodic boundary conditions were first implemented in MFIX as a part of the research reported by Agrawal et al.[1] and are now available for any user as a standard option for users.

Simulations were performed using fluid and particle properties listed in Table 1; these correspond to fluidization of standard fluid catalytic cracking (FCC) particles by air (same as in Igci et al.[3]). All results will be presented in dimensionless form. All quantities of interest are rendered dimensionless using the particle density (ρ_s), terminal settling velocity of the particle $(\mathbf{v}_t)$, and g as characteristic density, velocity, and acceleration, respectively. Igci et al.[3] found that dimensionless forms of the results obtained in this manner applied to other particle sizes (around the nominal value shown in Table 1). In what follows, we use capital letters and/or carets to denote dimensionless quantities

$$\tilde{\mathbf{V}}_i=\frac{\tilde{\mathbf{v}}_i}{\mathrm{v}_t},\quad \overline{S}_i=\overline{s}_i\frac{\mathrm{v}_t}{g},\quad \hat{P}_{i,\mathrm{fil}}=\frac{p_{i,\mathrm{fil}}}{\rho_s\mathrm{v}_t^2},\quad \hat{\mu}_{i,\mathrm{fil}}=\frac{g\mu_{i,\mathrm{fil}}}{\rho_s\mathrm{v}_t^3},\quad i=s,g. \tag{12}$$

The dimensionless slip velocity is written as $\tilde{\mathbf{V}}_{\mathrm{slip}}=|\tilde{\mathbf{V}}_g-\tilde{\mathbf{V}}_s|$.

Simulations were started from a slightly nonuniform state to expedite the development of inhomogeneous flow structures. After an initial transient period, the system reached a statistical steady state with persistent temporally and spatially inhomogeneous structures. We typically waited for at least 10 cycles of fluctuations in the domain-average slip velocity, with an essentially invariant mean value, before gathering data for filtering analysis. Snapshots of the flow field were collected at various times in this statistical steady state. (see Figure 2 in Igci et al.[3] for a sample snapshot.) These computational data were then filtered using filters of different sizes, binned in terms of the values of the markers used to classify the subfilter-scale state, and then averaged within each bin to obtain statistics of filtered quantities. Further details of the procedure for this filtering operation can be found in Igci et al.[3]

Results and Discussion

Filtered fluid-particle drag coefficient

Figure 1 shows a scatter plot of the fractional correction, H, to the fluid-particle drag coefficient at various filtered particle volume fractions. The correction H is defined as follows

$$H=1-\frac{\beta_{\mathrm{fil}}}{\beta_{\mathrm{micro}}\left(\overline{\phi}_s,|\tilde{\mathbf{v}}_g-\tilde{\mathbf{v}}_s|\right)};\qquad \beta_{\mathrm{fil}}=\frac{\beta_{\mathrm{micro}}\left(\phi_s,|\mathbf{v}_g-\mathbf{v}_s|\right)\left(\mathbf{v}_{gy}-\mathbf{v}_{sy}\right)-\phi'_s\frac{\partial p'_g}{\partial y}}{\left(\tilde{\mathbf{v}}_{gy}-\tilde{\mathbf{v}}_{sy}\right)} \tag{13}$$

Note that one can define the filtered drag coefficient by processing the drag force data in either the vertical or lateral direction. We found that nearly the same estimates for β_{fil} were obtained in both directions, but the data obtained from the vertical direction (indicated as y in the above equation) were less noisy and so we computed β_{fil} using only the y-component of the drag data. (As H involves a ratio of drag coefficients, there is no need to make drag coefficients dimensionless.)

Each point in Figure 1 corresponds to different combinations of filter size, $\tilde{\mathbf{v}}_{\mathrm{slip}}$ and $\overline{\phi}_s$, and so this figure can be thought of a projection of all the results in the plane shown. Each point in this figure represents the average of a large number of realizations. It is readily apparent that H varies over a wide range. $H=0$ corresponds to a homogeneous microstructure; the larger the value of H, the more inhomogeneous the subfilter-scale structure is. The results in this figure were obtained from a set of 10 simulations, each with a different domain-average particle volume fraction. The domain size and grid resolution used in the simulations are summarized in the figure caption. The solid line in this figure is an approximate envelope of all these points, henceforth referred to as $h_{\mathrm{env},1}(\overline{\phi}_s)$. The broken line represents a simpler envelope, $h_{\mathrm{env},2}(\overline{\phi}_s)$. Curve-fit expressions for

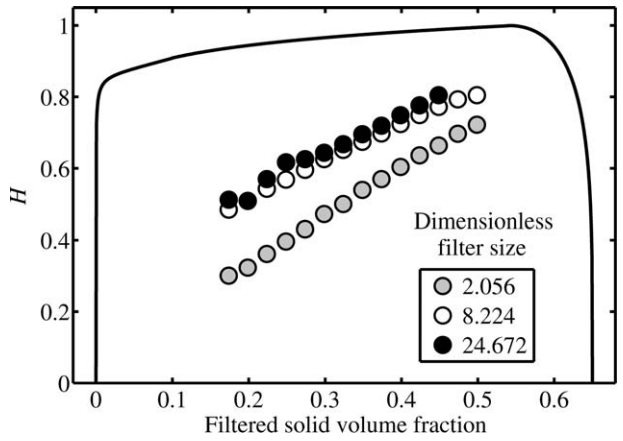

Figure 3. Correction to the drag coefficient (*H*) is plotted as a function of $\overline{\phi}_s$ for $\tilde{\mathbf{V}}_{slip}=0.6$ and three different filter sizes (indicated in the figure).

Also shown is the envelope $h_{env,1}(\overline{\phi}_s)$. The simulation conditions are as in Figure 1.

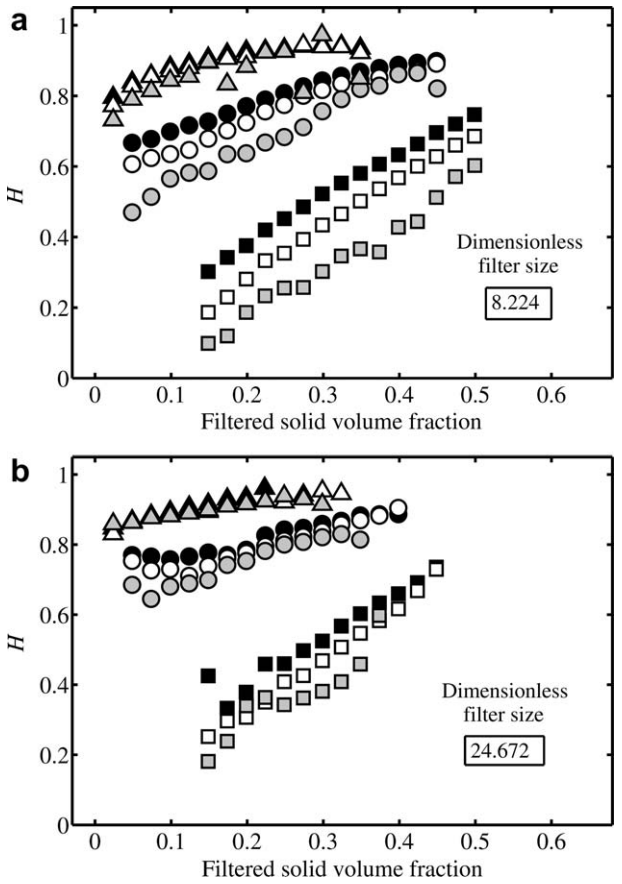

Figure 4. Correction to the drag coefficient (*H*) is plotted as a function of $\overline{\phi}_s$ for three different filtered slip velocities, and two different dimensionless filter sizes: 8.224 (a), 24.672 (b).

The dimensionless filtered slip velocities are 0.44 (□, ■), 1.60 (○, ●), and 4.80 (Δ, ▲). The simulation conditions except for the grid resolution, which is now varied, are as in Figure 1. The grid resolutions are 0.257 (black symbols), 0.514 (white symbols), and 1.028 (gray symbols).

$h_{env,1}(\overline{\phi}_s)$ and $h_{env,2}(\overline{\phi}_s)$ are presented in Table 2. The top left and right corners (in Figure 1) where these two envelopes differ are hardly sampled and, therefore, we do not anticipate a meaningful difference in the results obtained in filtered model simulations with these two different expressions. In our discussion below and in the figures that follow, we only present $h_{env,1}(\overline{\phi}_s)$ to illustrate that there is an envelope, and it is understood that we could have shown $h_{env,2}(\overline{\phi}_s)$ instead. It will become clear in the discussion below that $H=H(\overline{\phi}_s,\tilde{\mathbf{v}}_{slip},\Delta_f)$; here $\Delta_f=\frac{g\Delta_{fil}}{v_t^2}$ is the dimensionless filter size and Δ_{fil} is the dimensional filter size.

Figure 2 is obtained by averaging the results obtained at various slip velocities (by properly weighting them with their respective probabilities of occurrence). Such collapsed data, henceforth referred to as $\langle H\rangle(\overline{\phi}_s,\Delta_f)$, are precisely what Igci and Sundaresan[5] reported. Also shown in this figure is the $\langle H\rangle_{inf}(\overline{\phi}_s)$ reported by Igci and Sundaresan[5] for very large filter sizes. We are able to reproduce the earlier results, and so the trends discussed below represent additional insights gained in this study.

Figure 3 presents the value of H as a function of $\overline{\phi}_s$ for a specific value of $\tilde{\mathbf{v}}_{slip}$ and three different filter sizes, Δ_f. These represent a small subset of the results presented in Figure 1. The envelope $h_{env,1}(\overline{\phi}_s)$ is also included in this figure. It is readily apparent that H manifests a definitive trend with respect to the particle volume fraction for each filter size. (For the gas-particle system listed in Table 1, $\Delta_f=2.056$ corresponds $\Delta_{fil}=1\text{cm}$, which is $\sim 133\ d_p$.). As the filter size increases, the value of H increases, but it is clear that this change becomes less pronounced as the filter size increases.

Figures 4a, b show the influence of grid resolution on the value of H for two different filter sizes. In each of these figures, the results obtained at three different grid resolutions are presented for three different values of $\tilde{\mathbf{v}}_{slip}$. It is clear that the results do manifest noticeable grid dependence. The grid size dependence becomes weaker as the filtered gas-particle slip velocity and filter size increase. In any case, it is clear that it would be desirable to obtain better estimates of the values of H by extrapolating results of the type shown in this figure to infinite grid resolution. Constitutive models for H generated through such extrapolation will be presented later, but for now, we will present the results obtained at the highest resolution used in our study and illustrate the trends.

Figure 5a presents the variation of H with $\overline{\phi}_s$ for $\Delta_f=8.224$ and at several different $\tilde{\mathbf{V}}_{slip}$ along with $h_{env,1}(\overline{\phi}_s)$. The nearly linear variation of H with $\overline{\phi}_s$ is readily apparent at each $\tilde{\mathbf{v}}_{slip}$. At low slip velocities, the value of H is essentially zero at low $\overline{\phi}_s$ (the data are not shown for the sake of clarity), but deviates from zero at higher $\overline{\phi}_s$. As an example, for $\tilde{\mathbf{V}}_{slip}=0.24$, H is nearly zero for $\overline{\phi}_s$ below 0.2 and it increases linearly with after that. As the slip velocity increases, the data (and the corresponding lines) shift upward. Above some threshold value of slip velocity, the $H=0$ plateau at low $\overline{\phi}_s$ disappears, with the lines now starting on the left side of the envelope (e.g., see the results for $\tilde{\mathbf{V}}_{slip}=0.8$). At high $\overline{\phi}_s$, these lines terminate on the envelope. At very low and very high $\overline{\phi}_s$, the results become noisy (and hence are not shown, to keep the figure from getting too crowded), but they straddle the lines shown in this figure; so, these lines are indeed reasonable approximations.

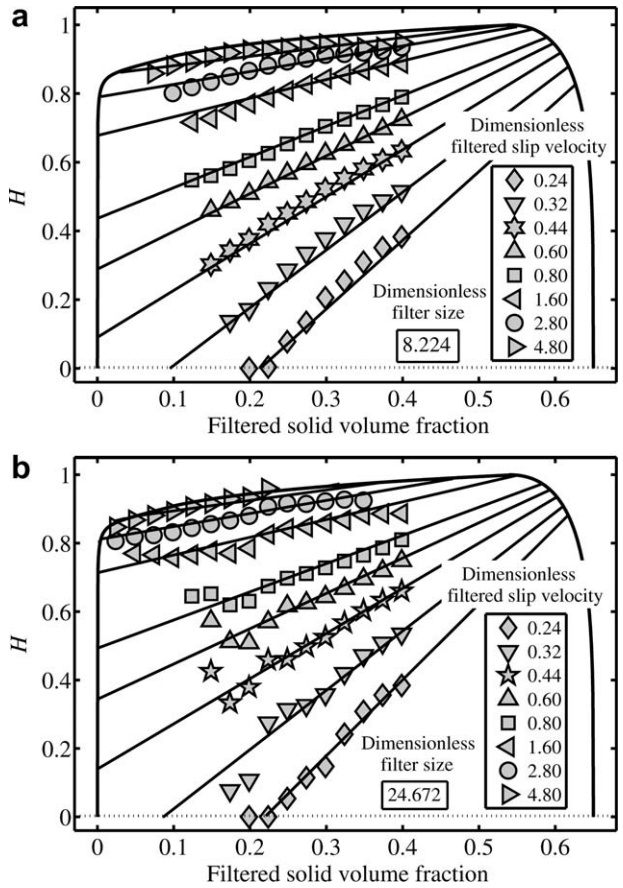

Figure 5. Correction to the drag coefficient (*H*) is plotted as a function of $\overline{\phi}_s$ for several filtered slip velocities, and two different dimensionless filter sizes: 8.224 (a) and 24.672 (b).

The simulation conditions are as in Figure 1.

Similar results are obtained for other filter sizes as well, and this is illustrated in Figure 5b corresponding to a larger filter size.

After ascertaining that the dependence of H on $\overline{\phi}_s$, $\tilde{\mathbf{V}}_{\text{slip}}$, and Δ_f is robust, closure for H was formulated by performing simulations at three different grid resolutions (as illustrated in Figures 4a, b), extrapolating the results to infinite resolution and then correlating the extrapolated results via simple analytical expressions. The resulting closure for H is summarized in Appendix A for several different dimensionless filter sizes. We have not sought to combine all these into a more compact form by explicitly correlating the filter size dependence of the coefficients. In Table 2, we have summarized the closure proposed for H for large filter sizes. In our 2-D simulations, H was found to become essentially independent of filter size for $\Delta_f >\sim 25$. Igci and Sundaresan[5] found that $\langle H\rangle_{\text{inf}}$ extracted from 2-D and 3-D simulations were essentially the same and that $\langle H\rangle$ became independent of Δ_f at smaller filter sizes in their 3-D calculations than in 2-D. Therefore, we anticipate that for 3-D simulations of most industrial-scale devices where the grid sizes tend to be large, an asymptotic limit should suffice and that the expressions in Table 2 should be reasonable first approximations, even though they were generated via 2-D simulations. (Strictly speaking, this remains to be verified by repeating this study in 3-D, but these are beyond our current resources.)

The variation of H manifested in Figures 2–5 deserves some discussion. First, the increase in H with Δ_f is entirely consistent with previous studies; the larger the filter size (at given $\overline{\phi}_s$ and $\tilde{\mathbf{V}}_{\text{slip}}$), the more inhomogeneous the subfilter-scale structure is. Second, we now find that at given filter size and $\overline{\phi}_s$, an increase in slip velocity leads to an increase in H, which is equivalent to a decrease in the filtered drag coefficient; at first, this appears to be counterintuitive, as in every drag coefficient correlation an increase in slip velocity increases the Reynolds number and increases the drag coefficient (e.g., see the widely used Wen–Yu[7] correlation). This result implies that the origin of the slip velocity dependence seen in Figures 3–5 is not inertial. We argue that the observed result is a consequence of the extent of subfilter-scale inhomogeneity; the larger the slip velocity, the greater the degree of segregation between the particles and the gas is and, hence, the lower the drag coefficient. In other words, the slip velocity (as a second marker) classifies the subfilter-scale structures into varying degrees of inhomogeneity. Third, at given slip velocity and filter size, H increases with $\overline{\phi}_s$ for most of the volume fraction range (except at nearly packed bed conditions). At very low slip velocities, little inhomogeneity develops at low $\overline{\phi}_s$ and H is virtually zero; the same level of slip velocity destabilizes the nearly homogeneous subfilter-scale structure at particle volume fractions above some threshold value. This threshold $\overline{\phi}_s$ decreases with increasing slip velocity, and above some critical value of slip velocity, inhomogeneous microstructure forms at all $\overline{\phi}_s$ values.

Although a wide range of particle volume fractions and slip velocities are captured in the statistical results presented in Figures 3–5, the region in the $\left(\overline{\phi}_s, \tilde{\mathbf{V}}_{\text{slip}}\right)$ space where most of the samples lie is clustered around the mean values: $\langle\tilde{\mathbf{V}}_{\text{slip}}\rangle = f\left(\overline{\phi}_s, \Delta_f\right)$. This is illustrated in the form of a gray-scale plot in Figure 6 for a specific filter size, where we present the probability distribution function of $\tilde{\mathbf{V}}_{\text{slip}}$ as a function of $\overline{\phi}_s$; also shown are $\langle\tilde{\mathbf{V}}_{\text{slip}}\rangle$. The mean slip velocity increases with $\overline{\phi}_s$ at first, indicating the formation of larger clusters; it then decreases with increasing $\overline{\phi}_s$, indicative of interaction between the clusters. At much larger $\overline{\phi}_s$ values, clusters give ways to bubbles, which become less and less prevalent as $\overline{\phi}_s$ increases. The shape of the curves in Figure 2 can now be understood. The initial increase in $\langle H\rangle$ (at low $\overline{\phi}_s$) comes from the initial increase in mean slip velocity. Subsequent gradual decline in $\langle H\rangle$ with increasing $\overline{\phi}_s$ comes from the decrease in mean slip velocity; $\langle H\rangle$ declines only gradually with $\overline{\phi}_s$ at intermediate values of $\overline{\phi}_s$, as the variation of H with $\tilde{\mathbf{V}}_{\text{slip}}$ is small at large $\tilde{\mathbf{V}}_{\text{slip}}$ values (see Figures 5a, b). At high $\overline{\phi}_s$, most of the samples occur at low slip velocities, and this is reflected by a rapid decrease in $\langle H\rangle$ (see Figure 6).

Filtered pressures and viscosities

The formation of clusters, streamers, and bubbles in fluidized suspensions stems from a gravity-driven instability; so, the intensity of velocity fluctuations can be expected to scale as $\mathbf{v}_t^2$, and the characteristic length will correspondingly scale as $\mathbf{v}_t^2/g$. For this reason, in our earlier studies, these scales were used to nondimensionalize the mesoscale normal stresses and viscosity (e.g., see Agrawal et al.[1]). In this study, based on our experience with the filtered drag

Table 2. $H=H\left(\overline{\phi}_s, \tilde{\mathbf{V}}_{\mathbf{slip}}\right)$ Applicable to Large Filter Sizes

$$H=\text{Min}\left(h_{\text{env},1} \text{ or } h_{\text{env},2},\ h_{\text{lin}}\right)$$

$$h_{\text{env},1} = \begin{cases} \dfrac{0.5643\left(1+\overline{\phi}_s\right)\left(\overline{\phi}_s\right)^{0.15}}{0.5766\left(\overline{\phi}_s\right)^{0.3} + 0.1997} & \text{for } \overline{\phi}_s \le 0.10 \\ 0.8428 + 0.6393\left(\overline{\phi}_s\right) - 0.6743\left(\overline{\phi}_s\right)^2 & \text{for } 0.10 < \overline{\phi}_s \le 0.54 \\ \dfrac{0.4099\left(0.65-\overline{\phi}_s\right)^{0.25}}{\left(\overline{\phi}_s\right)^{-0.25} - 0.9281} & \text{for } 0.54 < \overline{\phi}_s \le 0.65 \\ 0 & \text{for } \overline{\phi}_s > 0.65 \end{cases}$$

$$h_{\text{env},2} = 0.8428 + 0.6393\left(\overline{\phi}_s\right) - 0.6743\left(\overline{\phi}_s\right)^2 \quad \text{for } 0 \le \overline{\phi}_{ss} \le 0.65$$

$$h_{\text{lin}} = \begin{cases} f_{\text{inf}} \cdot h_1 & \text{for } h_1 > 0 \\ 0 & \text{for } h_1 < 0 \end{cases}$$

$$f_{\text{inf}} = 0.882\left(2.145 - \frac{7.8\left(\tilde{\mathbf{V}}_{\text{slip}}\right)^{1.8}}{7.746\left(\tilde{\mathbf{V}}_{\text{slip}}\right)^{1.8} + 0.5586}\right)$$

$$h_1 = \left(\frac{1.6\,\tilde{\mathbf{V}}_{\text{slip}} + 4}{7.9\,\tilde{\mathbf{V}}_{\text{slip}} + 0.08}\right)\overline{\phi}_s + \left(0.9394 - \frac{0.22}{0.6\,\tilde{\mathbf{V}}_{\text{slip}} + 0.01}\right)$$

Note: f_{inf} accounts for the extrapolation to infinite grid resolution.

coefficient discussed above, we first examined if the filtered slip velocity could serve as a second marker for the mesoscale pressures and viscosities; but, no systematic dependence of the mesoscale stresses on the filter slip velocity could be identified. However, we found that the scalar shear rates $S_i, i=s,g$ were indeed viable second markers for the mesoscale stresses in the two phases. (We also examined if the scalar shear rates could be used as a second marker for the filtered drag coefficient, but without success.) Specifically, we found that $\Delta_f^2 S_i^2$ captured the intensity of velocity fluctuations equally well or better when compared to $\mathbf{v}_t^2$. With this in mind, we advance in this study constitutive models for the mesoscale stresses based on $\Delta_f^2 S_i^2$, which is structurally identical to that of the well-known Smagorinsky[17] models for single-phase turbulent flows.

In our simulations, most of the contributions to the scalar shear rate (defined in Eq. 10) came from the deviatoric terms in $\overline{S}_i$. We simply write $\overline{S}_i=\overline{S}_i\left(\overline{\phi}_s, \Delta_f\right)$, as we could not identify a systematic dependence of the scalar shear rates on any second marker; for example, Figure 7 shows that the filtered slip velocity is not a useful second marker. The same holds for all the quantities described below. (In other words, we found a useful second marker only for the fluid-particle drag coefficient.)

Figures 8a, b show the filtered scalar shear rate of the particle and gas phases, respectively. The influence of grid resolution is illustrated for $\Delta_f=8.224$ in these figures. Unlike the fluid-particle drag coefficient, grid size dependence of quantities related to filtered stress were found to be much weaker; therefore, we have simply used the results obtained from the simulations at the highest resolution in our analysis below. Both gas and particle-phase scalar shear rates decrease with increasing particle volume fraction; the data at very low $\overline{\phi}_s$ tend to be more scattered and are not shown. In this specific

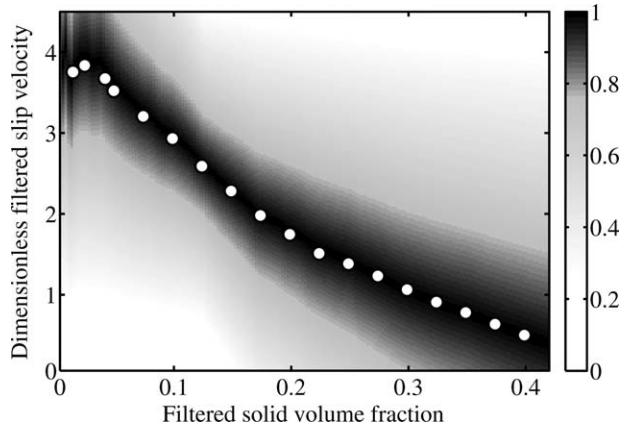

Figure 6. Grayscale plot of the probability distribution of the filtered slip velocity as a function of $\overline{\phi}_s$.

Also shown are the mean filtered slip velocity (○) values at several different $\overline{\phi}_s$ values. Dimensionless filter size = 24.672. The simulation conditions are as in Figure 1.

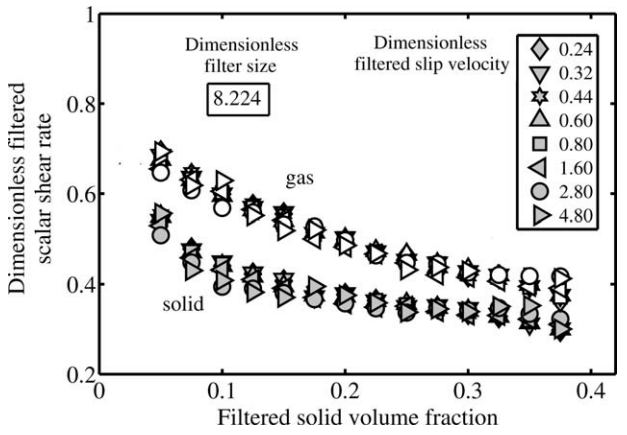

Figure 7. Dimensionless filtered scalar shear rates of gas and particle phases are plotted against $\overline{\phi}_s$.

Dimensionless filter size = 8.224. The simulation conditions are as in Figure 1. Results are shown for several different filtered slip velocities. The legends apply for both filled and unfilled symbols.

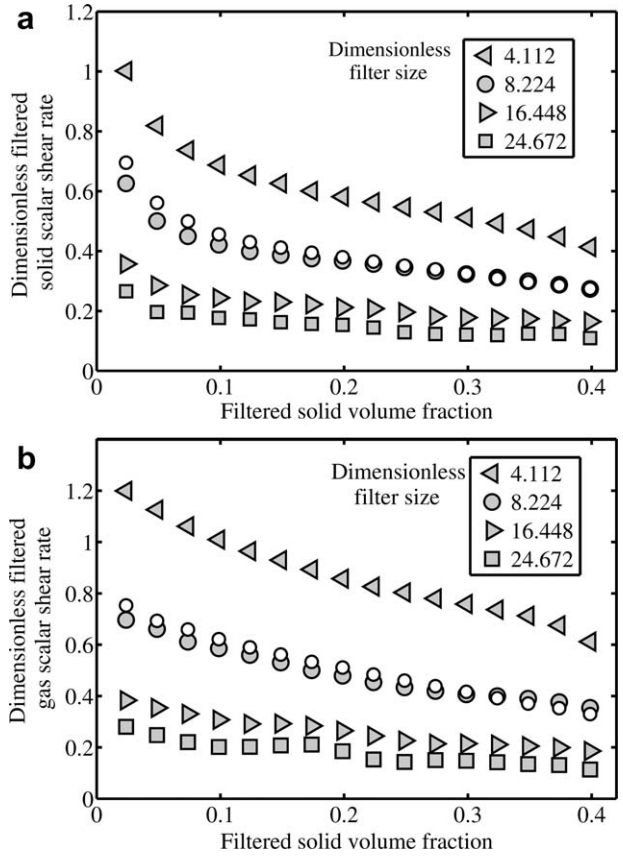

Figure 8. Dimensionless filtered scalar shear rate is plotted against $\overline{\phi}_s$ for four different dimensionless filter sizes for both phases: solid (a) and gas (b).

The simulation conditions are as in Figure 1 for the points denoted by gray symbols. The open symbols (○) correspond to a coarser grid (with a resolution of 0.514) and a dimensionless filter size of 8.224.

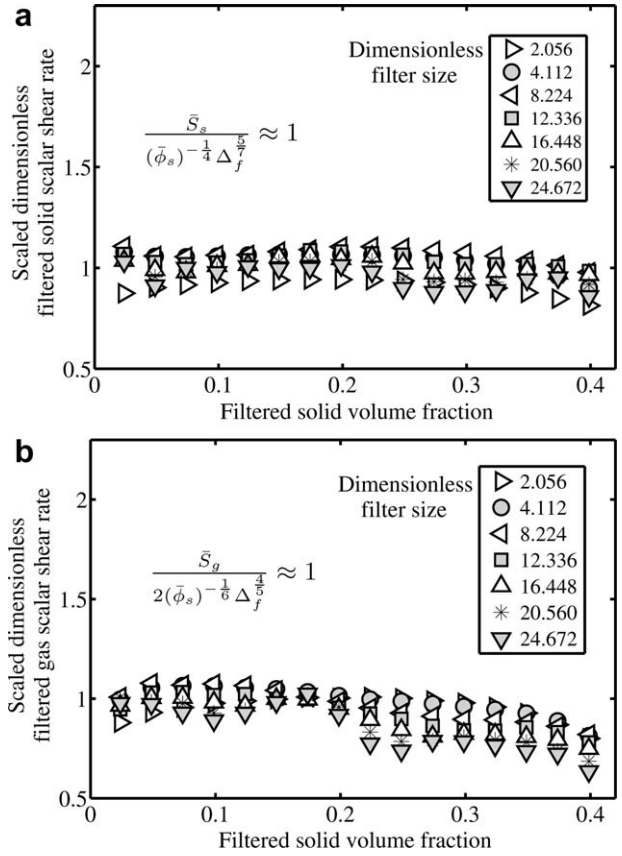

Figure 9. Scaled filtered scalar shear rate as a function of $\overline{\phi}_s$, for both phases: solid (a) and gas (b).

The simulation conditions are as in Figure 1. Results are shown for several different filter sizes.

problem, in the limit $\overline{\phi}_s \to 0$, the fluctuations will disappear and we should recover fluid statics. Therefore, it seems reasonable to anticipate that both scalar shear rates should go to zero as $\overline{\phi}_s \to 0$; however, the peak in the scalar shear rates appears to be at $\overline{\phi}_s$ below the range shown in these figures. Over the range of $\overline{\phi}_s$ values shown in these figures, the (dimensionless) scalar shear rates could be captured adequately as

$$\frac{\overline{S}_s}{\left(\overline{\phi}_s\right)^{-\frac{1}{4}}\Delta_f^{-\frac{5}{7}}} \approx 1; \qquad \frac{\overline{S}_g}{2\left(\overline{\phi}_s\right)^{-\frac{1}{6}}\Delta_f^{-\frac{4}{5}}} \approx 1 \tag{14}$$

The quantities on the left hand side, henceforth referred to as scaled scalar shear rate, are presented in Figures 9a, b, respectively.

Figures 10a, b present the variation of $\hat{P}_{s,\mathrm{fil}}$ and $\hat{\mu}_{s,\mathrm{fil}}$ with $\overline{\phi}_s$ for various filter sizes, respectively. Similar figures can be found in Igci et al.[3] as well. $\hat{P}_{s,\mathrm{fil}}$ manifests some grid size dependence, and so if one sets out to write a model for it in terms of $\overline{\phi}_s$ and Δ_f, extrapolation to infinite resolution appears warranted. However, we found that an alternate model in terms of $\overline{S_s}$, $\overline{\phi}_s$ and Δ_f showed much less grid size dependence and so we simply retain the results obtained in the highest resolution simulations.

Figures 11a, b present variation of $\hat{P}_{g,\mathrm{fil}}$ and $\hat{\mu}_{g,\mathrm{fil}}$ with $\overline{\phi}_s$ for various filter sizes, respectively. The large difference in the typical magnitudes shown in Figures 10a and 11a stem from the differences in the densities of the two phases; furthermore, their $\overline{\phi}_s$ dependence is qualitatively different. The same is true for the viscosities as well—compare Figures 10b and 11b. The data shown in Figures 10 and 11 manifest smooth trends for modest filter sizes, but become somewhat irregular for larger filter sizes; this is attributed to comparatively poorer statistics. It can readily be concluded from the typical magnitudes of the filtered viscosities of the gas and particle phases that the filtered deviatoric stress in the gas phase plays a much weaker role than that in the particle phase.

Drawing inspiration from single-phase turbulence literature,[12,17] we examined the suitability of a different constitutive model for the filtered viscosities, which in dimensionless form can be written as

$$\hat{\mu}_{s,\mathrm{fil}} = C_{\mathrm{visc,s}}\Delta_f^2\overline{S_s}, \quad \hat{\mu}_{g,\mathrm{fil}} = C_{\mathrm{visc,g}}\frac{\rho_g}{\rho_s}\Delta_f^2\overline{S_g} \tag{15}$$

It is readily apparent from Figures 12a, b that such models work well for the subfilter-scale viscosities. For the range of conditions presented, $C_{\mathrm{visc,s}} = 0.105\,\overline{\phi}_s$ and $C_{\mathrm{visc,g}} = 0.17 - 0.275\,\overline{\phi}_s$ capture the data for several different filter sizes reasonably well. In these plots, the results obtained with grids that are twice as long in each direction collapsed almost exactly over the data presented. This confirms that the grid size dependence seen in Figures 10 and

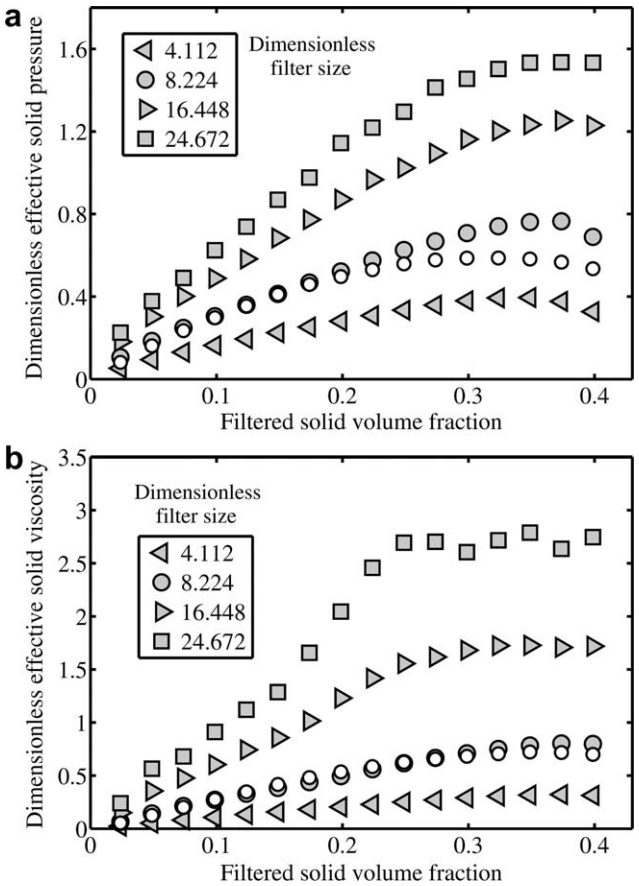

Figure 10. Dependence of the effective solid-phase pressure (a) and viscosity (b) arising from subfilter-scale fluctuations on $\overline{\phi}_s$ for various filter sizes.

The simulation conditions are as in Figure 1 for the points denoted by gray symbols. The open symbols (○) correspond to a coarser grid (with a resolution of 0.514) and a dimensionless filter size of 8.224.

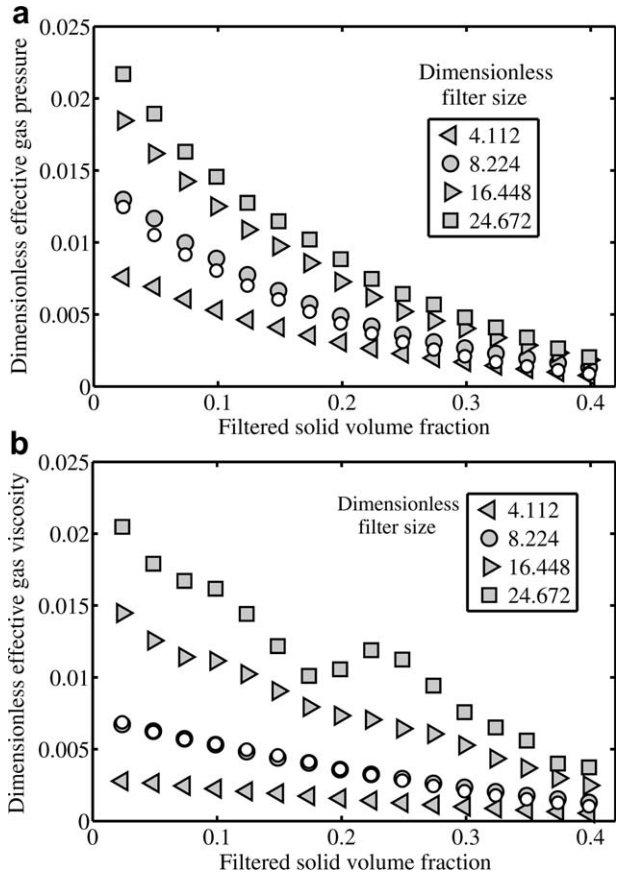

Figure 11. Dependence of the effective gas-phase pressure (a) and viscosity (b) arising from subfilter-scale fluctuations on $\overline{\phi}_s$ for various filter sizes.

The simulation conditions are as in Figure 1 for the points denoted by gray symbols. The open symbols (○) correspond to a coarser grid (with a resolution of 0.514) and a dimensionless filter size of 8.224.

11 can be attributed to the grid size dependence of the estimated values of the scalar shear rates.

It was found that $\hat{P}_{s,\mathrm{fil}}$ and $\hat{P}_{g,\mathrm{fil}}$ could also be modeled in terms of the shear rates, but with slightly different dependence on the dimensionless filter size

$$\hat{P}_{s,\mathrm{fil}} = C_{\mathrm{press,s}} \Delta_f^{16/7} \overline{S}_s^2, \quad \hat{P}_{g,\mathrm{fil}} = C_{\mathrm{press,g}} \frac{\rho_g}{\rho_s} \Delta_f^{16/7} \overline{S}_g^2 \qquad (16)$$

Figures 13a, b demonstrate that these models work reasonably well with $C_{\mathrm{press,s}} = 0.17 \quad \overline{\phi}_s$ and $C_{\mathrm{press,g}} = 0.275 - 0.44 \quad \overline{\phi}_s$.

One can readily ascertain the correspondence between the new constitutive models proposed here and those suggested by Igci and Sundaresan.[5] On combining Eqs. 14–16, we find that $\hat{P}_{s,\mathrm{fil}} \sim \Delta_f^{6/7}$ and $\hat{\mu}_{s,\mathrm{fil}} \sim \Delta_f^{9/7}$, and these exponents are very close to those reported by Igci and Sundaresan.[5] The simpler models proposed by Igci and Sundaresan[5] postulate that the subfilter-scale corrections to the dimensionless pressure and viscosity (for a given filter size) depend only on $\overline{\phi}_s$ (which is a dynamically evolving quantity in the simulation of the filtered model with a specific filter size), whereas the present model allows these quantities to vary with both $\overline{\phi}_s$ and $\overline{S}_i, i=s,g$ (two dynamically evolving quantities). As in the case of the filtered fluid-particle drag coefficient, the new expressions, therefore, permit a better classification of the relation between subfilter-scale corrections and the filtered fields; this could improve the accuracy of the predictions afforded by the filtered model.

Before we close our discussion, it should be noted that all of our highly resolved simulations, which formed the basis for our filtered constitutive models, were done in periodic domains. As every point in a periodic domain is statistically equivalent to every other point, we could gather efficiently a large amount of statistics needed for filtered constitutive model development. Igci and Sundaresan[4] performed a series of highly resolved simulations in the presence of bounding walls, which were computationally more expensive, and found the following

1. In the core region (away from the walls), the filtered model developed using periodic boundary conditions worked very well.
2. In the vicinity of bounding walls, corrections had to be introduced to the filtered constitutive models.

As a result, we chose to begin our search for improved filtered constitutive models first with periodic domains and then examine in future studies if they need to be refined in

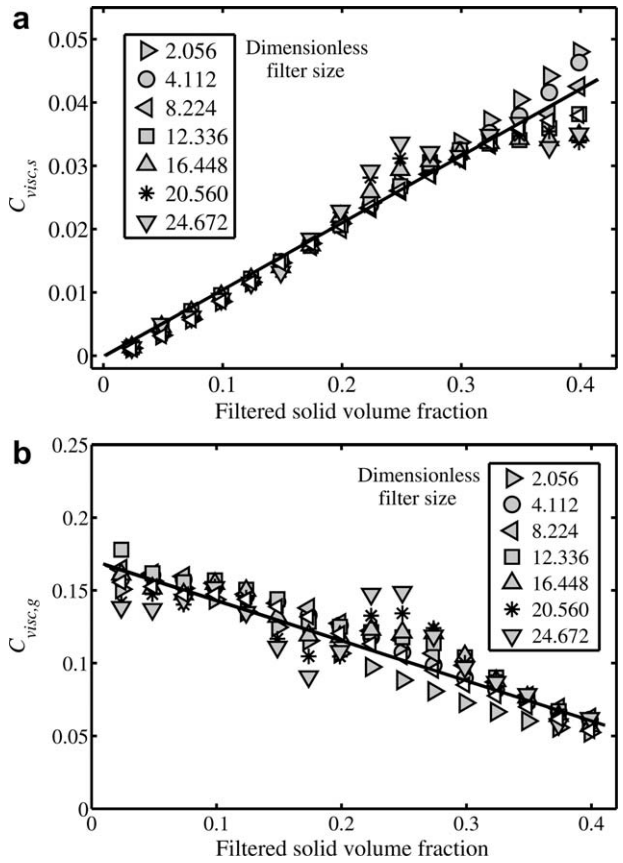

Figure 12. Effective viscosity coefficient is plotted against $\overline{\phi}_s$ for the two phases: solid (a) and gas (b).

Results are presented for several different filter sizes. The simulation conditions are as in Figure 1 for the points denoted by gray symbols. The open symbols (◁) correspond to a coarser grid (with a resolution of 0.514) and a dimensionless filter size of 8.224.

the vicinity of boundaries. Strictly speaking, the models presented in this manuscript may very well need wall corrections, just as the previous-generation model did. However, we suspect that the need for wall correction to the drag coefficient in the new model proposed here will be less pronounced, as it includes one additional subfilter-scale quantity, namely, the filtered slip velocity. Filtered slip velocities in the wall region extracted from highly resolved simulations of wall-bounded flow were found by Igci and Sundaresan[4] to be larger than those in the core (at comparable filtered particle fractions); to account for it, they needed to lower in an empirical manner the filtered drag coefficient near the wall (when compared to the expression used in the core region). With the present model, however, a larger slip velocity (say, in the vicinity of the wall) will automatically lead to a lower drag coefficient! Thus, we suspect that the new model may not need further empirical wall correction; however, this is only a speculation at the present time and further studies are needed to verify it.

The new constitutive relations for the stresses take the form of Smagorinsky[17] subgrid model for turbulent stresses. Dynamic subgrid models based on test filters and the Smagorinsky subgrid model for turbulent stresses have been successfully applied in single-phase turbulent flows[18] and its use for two-phase flows has been discussed by Parmentier et al.[8] The need for wall correction is mitigated by the use of such dynamic models; we see this as an attractive way of proceeding in the future and sidestepping the need to introduce wall corrections for the stresses.

Summary

Gas-particle flows in turbulent and circulating fluidized beds involve persistent fluctuations over a wide range of length and time scales. Resolving all these fluctuations in simulations is not practical. Filtered models that can be solved to capture the coarser flow structures are more useful, but they require constitutive models to account for the influence of subfilter-scale fluctuations. Such constitutive models are beginning to emerge in the literature.

In this study, we have carried out a large number of highly resolved simulations of a kinetic theory-based TFM in 2-D periodic domains and systematically filtered the data. Specifically, we examined several possible markers that can be used to classify the inhomogeneous subfilter-scale structures that can occur. It is demonstrated that the correction to the drag coefficient should depend not only on the filter size and filtered particle volume fraction, but also on the filtered slip velocity. The filtered drag coefficient decreases with increasing slip velocity, which rules out inertial correction as the explanation for the slip-velocity dependence; it is argued that as the slip velocity increases, the subfilter-scale structure

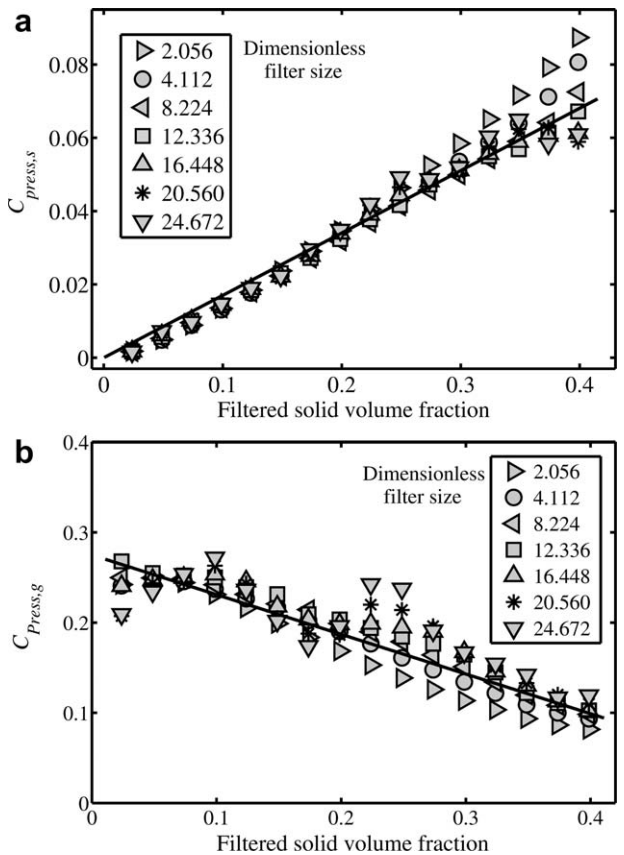

Figure 13. Effective pressure coefficient is plotted against $\overline{\phi}_s$ for the two phases: solid (a) and gas (b).

Results are presented for several different filter sizes. The simulation conditions are as in Figure 1.

becomes more and more inhomogeneous. For large filter sizes, the correction to the drag coefficient appears to become independent of the filter size. A model for this asymptotic correction, which is only a function of the particle volume fraction and dimensionless slip velocity is presented. For most simulations of industrial-scale devices where the grid sizes tend to be large, this asymptotic limit should suffice.

The corrections to the pressure and viscosity (of each phase) arising from the subfilter-scale fluctuations are now expressed in terms of the filter size, filtered particle volume fraction, and the filtered (i.e., resolved) scalar shear rates; the forms of these new models are reminiscent of the classical Smagorinsky[17] models in single-phase turbulent flows. Dynamic models via test filter approach, widely used in large-eddy simulations of single-phase turbulent flows[18] and adapted to the gas-particle flow problems by Parmentier et al.,[8] can readily be designed for these models, and may yield further improvements in the predictions of the filtered models.

Acknowledgments

S.S. acknowledges the financial support for this work from the Department of Energy—Carbon Capture Simulation Initiative and ExxonMobil Research and Engineering Co. C.C.M. and F.E.M. are grateful for the financial support from the São Paulo Research Foundation—FAPESP (Brazil), which allowed them to pursue this research at Princeton University.

Disclaimer

Appendix

Here, we summarize expressions for the correction $H = H\left(\overline{\phi}_s, \tilde{\mathbf{V}}_{slip}, \Delta_f\right)$ for several different dimensionless filter sizes. As discussed in the main text, these results were generated by performing simulations at three different grid resolutions and extrapolating them to infinite grid resolution (using a Richardson extrapolation following the work of Holloway and Sundaresan[19])

$$H = \text{Min}\left(h_{\text{env},1} \text{ or } h_{\text{env},2},\, h_{\text{lin}}\right)$$

The expressions for $h_{\text{env},1}$ and $h_{\text{env},2}$ can be found in Table 2

$$h_{\text{lin}} = \begin{cases} f_{\text{ext}} \cdot h_1 & \text{for} \quad h_1 > 0 \\ 0 & \text{for} \quad h_1 < 0 \end{cases}$$

The extrapolation to infinite resolution is captured by

$$f_{\text{ext}} = \left(\frac{3.494}{1+8\left(\Delta_f\right)^{0.4}} + 0.882\right) f_{\text{inf}}$$

where f_{inf} can be found in Table 2. The function h_1 for various filter sizes are summarized below

For $\Delta_f = 1.028$

$$h_1 = \left(1.076 + 0.12 \quad \tilde{\mathbf{V}}_{\text{slip}} - \frac{0.02}{\tilde{\mathbf{V}}_{\text{slip}} + 0.01}\right) \overline{\phi}_s + \left(0.084 + 0.09 \quad \tilde{\mathbf{V}}_{\text{slip}} - \frac{0.01}{0.1 \quad \tilde{\mathbf{V}}_{\text{slip}} + 0.01}\right)$$

For $\Delta_f = 2.056$

$$h_1 = \left(1.268 - 0.2 \quad \tilde{\mathbf{V}}_{\text{slip}} + \frac{0.14}{\tilde{\mathbf{V}}_{\text{slip}} + 0.01}\right) \overline{\phi}_s + \left(0.385 + 0.09 \quad \tilde{\mathbf{V}}_{\text{slip}} - \frac{0.05}{0.2 \quad \tilde{\mathbf{V}}_{\text{slip}} + 0.01}\right)$$

For $\Delta_f = 4.112$

$$h_1 = \left(\frac{0.018\tilde{\mathbf{V}}_{\text{slip}} + 0.1}{0.14\tilde{\mathbf{V}}_{\text{slip}} + 0.01}\right) \quad \overline{\phi}_s + \left(0.9454 - \frac{0.09}{0.2 \quad \tilde{\mathbf{V}}_{\text{slip}} + 0.01}\right)$$

For $\Delta_f = 8.224$

$$h_1 = \left(\frac{0.05\tilde{\mathbf{V}}_{\text{slip}} + 0.3}{0.4\tilde{\mathbf{V}}_{\text{slip}} + 0.06}\right) \quad \overline{\phi}_s + \left(0.9466 - \frac{0.05}{0.11 \quad \tilde{\mathbf{V}}_{\text{slip}} + 0.01}\right)$$

For $\Delta_f = 12.336$

$$h_1 = \left(\frac{1.3\tilde{\mathbf{V}}_{\text{slip}} + 2.2}{5.2\tilde{\mathbf{V}}_{\text{slip}} + 0.07}\right) \quad \overline{\phi}_s + \left(0.9363 - \frac{0.11}{0.3 \quad \tilde{\mathbf{V}}_{\text{slip}} + 0.01}\right)$$

For $\Delta_f = 16.448$

$$h_1 = \left(\frac{2.6\tilde{\mathbf{V}}_{\text{slip}} + 4}{10\tilde{\mathbf{V}}_{\text{slip}} + 0.08}\right) \quad \overline{\phi}_s + \left(0.926 - \frac{0.17}{0.5 \quad \tilde{\mathbf{V}}_{\text{slip}} + 0.01}\right)$$

For $\Delta_f = 20.560$

$$h_1 = \left(\frac{2.5\tilde{\mathbf{V}}_{\text{slip}} + 4}{10\tilde{\mathbf{V}}_{\text{slip}} + 0.08}\right) \quad \overline{\phi}_s + \left(0.9261 - \frac{0.17}{0.5 \quad \tilde{\mathbf{V}}_{\text{slip}} + 0.01}\right)$$

Notation

C_{press} = effective pressure coefficient
C_{visc} = effective viscosity coefficient
d = particle diameter, m
e_p = coefficient of restitution
g, $\mathbf{g}$ = acceleration due to gravity, m/s^2
h_{env} = envelop of all H points
H = correction factor for the fluid - particle drag coefficient
$\langle H \rangle$ = correction factor H collapsed over different values of slip velocity
$\langle H \rangle_{\text{inf}}$ = correction factor H colpased over different slip velocities for very large filters

$\boldsymbol{I}$ = unit tensor
$p_{i,\mathrm{fil}}$ = contribution to the filtered phase pressure arising from sub-filter scale fluctuations kg/m s^2
$\overline{p}_i$ = filtered phase pressure kg/m s^2
$\hat{P}_{i,\mathrm{fil}}$ = dimensionless equivalent of $p_{i,\mathrm{fil}}$
p'_g = fluctuation in gas phase pressure kg/m s^2
$\overline{\hat{s}i}$ = filtered rate of deformation of phase i S^{-1}
$\overline{S}_i$ = dimensionless equivalent of $\overline{s}_i$
$\mathbf{v}_i$ = local-averaged velocity of phase i in the microscopic two fluid model, m/s
v_{iy} = local-averaged velocity of phase i in the vertical direction, m/s
$\tilde{\mathbf{v}}_i$ = Favre-averaged velocity of phase i in the vertical direction, m/s
$\tilde{\mathbf{v}}_i$ = Favre-averaged velocity of phase i, m/s
$\tilde{\mathbf{V}}_i$ = dimensionless Favre-averaged velocity of phase i
$\mathbf{v}'_i$ = fluctuation in velocity of phase i m/s
$\tilde{\mathbf{v}}_{\mathrm{slip}}$ = dimensionless Favre - averaged slip velocity, m/s
v_t = terminal settling velocity, m/s

Greek letters

β_{micro} = drag coefficient in the microscopic two - fluid model, kg/m^3 s
β_{fil} = filtered drag coefficient, kg/m^3 s
ϕ_i = phase volume fraction
$\overline{\phi}_i$ = filtered phase volume fraction
ϕ'_i = fluctuation in phase volume fraction
ρ_i = phase density, kg/m^3
Δ_f = dimensionless filter size
Δ_{fill} = dimensional filter size
σ_i = stress tensor in the microscopic two - fluid model, kg/m s^2
$\overline{\sigma}_i$ = filtered stress tensor, kg/m s^2
σ'_i = fluctuation in stress tensor, kg/m s^2
$\overline{\sum_{i,\mathrm{fil}}}$ = contribution to the filtered phase stress arising from sub-filter scale fluctuations, kg/m s^2
$\mu_{i,\mathrm{fill}}$ = filtered phase viscosity, kg/m s
$\hat{\mu}_{i,\mathrm{fil}}$ = effective dimensionless phase viscosity

Subscripts

env = envelope
g = gas phase
i = gas or solid phase
fil = filtered
micro = microscopic
s = solid phase

Literature Cited

1. Agrawal K, Loezos PN, Syamlal M, Sundaresan S. The role of mesoscale structures in rapid gas-solid flows. *J Fluid Mech.* 2001;445:151–185.
2. Andrews AT IV, Loezos PN, Sundaresan S. Coarse-grid simulation of gas-particle flows in vertical risers. *Ind Eng Chem Res.* 2005;44:6022–6037.
3. Igci Y, Andrews AT IV, Sundaresan S, Pannala S, O'Brien T. Filtered two-fluid models for fluidized gas-particle suspensions. *AIChE J*. 2008;54:1431–1448.
4. Igci Y, Sundaresan S. Verification of filtered two-Fluid models for gas-particle flows in risers. *AIChE J*. 2011;57:2691–2707.
5. Igci Y, Sundaresan S. Constitutive models for filtered two-fluid models of fluidized gas-particle flows. *Ind Eng Chem Res.* 2011;50:13190–13201.
6. Igci Y, Pannala S, Benyahia S, Sundaresan S. Validation studies on filtered model equations for gas-particle flows in risers. *Ind Eng Chem Res.* 2012;51:2094–2103.
7. Wen CY, Yu YH. Mechanics of fluidization. *Chem Eng Prog Symp Ser.* 1966;62:100–111.
8. Parmentier J-F, Simonin O, Delsart O. A functional subgrid drift velocity model for filtered drag prediction in dense fluidized bed. *AIChE J*. 2012;58:1084–1098.
9. Li, J, Kwauk M. Particle-Fluid Two-Phase Flow: Energy-Minimization Multiscale Method. Beijing, P.R. China: Metallurgical Industry Press, 1994.
10. Shi Z, Wang W, Li J. A bubble-based EMMS model for gas–solid bubbling fluidization. *Chem Eng Sci.* 2011;66:5541–5555.
11. Hong K, Wang W, Zhou Q, Wang J, Ji L. An EMMS-based multi-fluid model for heterogeneous gas-solid riser flows: Part I. Formulation of structure-dependent conservation equations. *Chem Eng Sci.* 2012;75:376–389.
12. Pope SB. Turbulent flows. Cambridge, UK: Cambridge University Press, 2000.
13. Lun CKK, Savage SB, Jeffrey DJ, Chepurniy N. Kinetic theories of granular flows: inelastic particles in Couette flow and slightly inelastic particles in a general flow field. *J Fluid Mech.* 1984;140:223–256.
14. Gidaspow D. Multiphase Flow and Fluidization. San Diego, CA: Academic Press, 1994.
15. Koch DL, Sangani AS. Particle pressure and marginal stability limits for a homogeneous monodisperse gas fluidized bed: kinetic theory and numerical simulations. *J Fluid Mech.* 1999;400:229–263.
16. Syamlal M, Rogers W, O'Brien T. MFIX Documentation. Morgantown, WV: U.S. Department of Energy, Federal Energy Technology Center, 1993.
17. Smagorinsky J. General circulation experiments with the primitive equations. *Mon Weather Rev.* 1963;91:99–164.
18. Germano M, Piomelli U, Moin P, Cabot WH. A dynamic subgrid-scale eddy viscosity model. *Phys Fluids A.* 1991;3:1760–1765.
19. Holloway W, Sundaresan S. Filtered models for reacting gas-particle flows. *Chem Eng Sci.* 2012;82:132–143.

Manuscript received Oct. 26, 2012, and revision received Feb. 25, 2013.